

International Journal of Thin Films Science and Technology

http://dx.doi.org/10.18576/ijtfst/140310

Applying the Sestak-Berggren Model to Analyze Non-Isothermal Kinetics and Thermodynamics of LiMnPO₄ Synthesized from NH₄MnPO₄·H₂O and Li₂CO₃

Safya Taha ¹, E. R. Shaabn ^{1,*}, M. Moustafa Abdel-Rahim ², Abdelaziz M. Aboraia ¹

Received: 3 Feb. 2025, Revised: 18 Aug. 2025, Accepted: 25 Aug. 2025

Published online: 1 Sep. 2025

Abstract: This study details the synthesis, thermal characterization, and kinetic analysis of lithium manganese phosphate (LiMnPO₄), a material of significant interest for energy storage applications. LiMnPO₄ was synthesized through a multi-step process involving the precipitation of ammonium manganese phosphate hydrate (NH₄MnPO₄·H₂O) followed by a solid-state reaction with lithium carbonate (Li₂CO₃). The reaction conditions were optimized through thermogravimetric (TGA) and differential thermal analysis (DTA), identifying critical phase transformation temperatures. Calcination at 600 K, 730 K, and 840 K resulted in distinct crystalline phases, as confirmed by X-ray diffraction (XRD) and Fourier-transform infrared (FTIR) spectroscopy. Thermal behavior was further investigated to determine activation energies for phase transitions using the Kissinger-Akahira-Sunose (KAS) and Šesták-Berggren (SB) models. The KAS analysis revealed activation energies of 137.95 and 318.70 kJ/mol for sequential phase transitions, corresponding to dehydration and LiMnPO₄ formation. FTIR analysis demonstrated significant changes in vibrational modes, indicating structural evolution during heating. SB modeling effectively described the reaction kinetics, providing insights into nucleation and growth mechanisms, with kinetic parameters suggesting three-dimensional volume nucleation as the dominant mechanism. These findings elucidate the thermal and kinetic characteristics of NH₄MnPO₄·H₂O to LiMnPO₄ conversion, offering a robust framework for optimizing synthesis conditions and improving material performance for electrochemical applications.

Keywords: Solid-state synthesis, Thermal analysis (TGA/DTA), Kinetic modeling (Kissinger and Šesták-Berggren), Phase transformation.

1 Introduction

Solid-state reaction kinetics have been extensively explored using thermal analysis methods, with significant advances in both experimental and computational methodologies permitting more accurate kinetic parameter extraction. However, the deconvolution of overlapped thermal events has always relied on the skill of experienced practitioners, with a judgment based on equipment experience and chemistry interpretation influencing the amount of thermal events assigned [1,2]. Many approaches have been developed to concurrently deconvolve a statistically meaningful number of heat events and retrieve kinetic information, as detailed in specialized publications. Sestak-Berggren model, which describes the concepts of modeling the kinetics of solid-state reactions by fitting numerous peak curves at the same time, is one of the most commonly used methodologies. Mathematically, this model provides an indicator of the mechanism in action and allows kinetic parameters such as activation energy to be calculated [2,3,4].

Such a methodology is proven using in silico thermo-conductivity detector (TCD) data, which indicate the Šesták-Berggren modeling approach's internal consistency, adaptability to noisy data, and ability to predict mechanisms occurring during a thermally driven solid-state reaction. Using these in silico data, it was demonstrated that Šesták-Berggren model can separate overlapped peaks without requiring a priori peak deconvolution [1,2,3,4,5,6]. In other words, the Šesták-Berggren (SB) model is commonly used in thermal analysis to evaluate material degradation, crystallization, and reaction kinetics. Its adaptability makes it ideal for investigating functionalized materials, particularly

¹ Physics Department, Faculty of Science, Al-Azhar University, Assiut 71524, Egypt

² Physics Department, faculty of Science, Assiut University, Assiut 7115, Egypt

^{*} Corresponding author e-mail: esamramadan2008@gmail.com



for modeling complex reaction pathways that simpler kinetic models cannot. Table 1 Šesták-Berggren-model equation and the physical significance of each of its parts [7,8,9].

SB-model	$\frac{d\chi}{dt} = K_0 e^{-\frac{L_a}{RT}} \chi^m (1 - \chi)^n f(T)$
χ	An extent of reaction represents the fraction of the material that has undergone the reaction at
	the time. The value of such exponent enclosed in between 0 and 1, where 0 means no reaction
	while 1 means reaction completed
t, s	The time which is the independent variable over which the reaction progresses
$\frac{\frac{d\chi}{dt'}s^{-1}}{K_o, s^{-1}}$	The reaction rate: the change in the extent of reaction (χ) per unit time.
$K_o, {\rm s}^{-1}$	The frequency factor: reflects the frequency of successful collisions or transitions leading to
	reaction.
$e^{-\frac{E_a}{RT}}$	The Arrhenius term: accounting for the temperature (T)-dependent probability of overcoming
	the energy barrier E_a . Where R is the gas constant.
χ^m	The dependence of the reaction rate on the extent of reaction, modeling processes like
	autocatalysis.
m	m : Reaction exponent that modifies the role of α in the rate law
$(1-\chi)^n$	The unreacted fraction's contribution to the reaction rate, often linked to depletion or inhibition
	effects.
2	Reaction/kinetic exponent representing the influence of the unreacted material
f(T)	A temperature-dependent function may incorporate system-specific terms such as phase
	transitions or thermal effects. If the Arrhenius term completely captures temperature
	dependency, it is frequently eliminated in simpler applications.

Table 1: SB-model equation and the physical significance of each of its parts

Such a model can determine the activation energy (E_a) , pre-exponential factor (A), and reaction sequence of functionalized materials, which are commonly destroyed or converted under heat. This provides insights into their thermal stability. Furthermore, the SB model can assist in characterizing activation pathways by illustrating how surface alterations influence reaction kinetics. Finally, the SB model enables a direct comparison of kinetic parameters between functionalized and non-functionalized counterparts, emphasizing the role of functional groups or coatings [1,7,8,9].

This study uses the Šesták-Berggren (SB) model to analyze the non-isothermal kinetics and thermodynamics of NH₄MnPO₄·H₂O and Li₂CO₃. The focus is on understanding the reaction mechanism, activation energy, and thermal stability. LiMnPO₄ was synthesized from NH₄MnPO₄ · H₂O and Li₂CO₃ using a solid-state technique, and its thermal breakdown and phase formation were described using the SB model. The kinetic parameters and thermodynamic properties were then assessed to see how the material's functional performance related to its synthesis circumstances.

2 Experimental Work

2.1 Procedures of LiMnPO₄ synthesis

0.5 M solution of manganese chloride tetrahydrate (MnCl₂·4H₂O) was prepared as the manganese precursor. To this solution, an excess amount of a saturated, 10 M solution of ammonium hydrogen phosphate ((NH₄)₂HPO₄) was added slowly under constant stirring. The resulting mixture was allowed to react, forming a precipitate of ammonium manganese phosphate hydrate (NH₄MnPO₄ · H₂O). The precipitate was then aged at $90 \pm 5^{\circ}$ C for 1 hour in an air-circulating oven. Following the aging step, the product was filtered, and the residue was washed several times with deionized (DI) water to remove any soluble by-products or unreacted ions.

The washed solid was then dried in a desiccator to remove any residual moisture and to ensure complete drying of the $NH_4MnPO_4 \cdot H_2O$. The synthesized $NH_4MnPO_4 \cdot H_2O$ was then subjected to a solid-state conversion to lithium manganese phosphate (LiMnPO₄) by reaction with lithium carbonate (Li₂CO₃). Stoichiometric amounts of Li₂CO₃ (99% purity, Fluka) and the previously synthesized NH₄MnPO₄ · H₂O were carefully weighed and finely ground together in a mortar for 30 minutes to achieve a homogeneous mixture.

A small portion of the mixture was analyzed by Thermogravimetric Analysis (TGA) and Differential Thermal Analysis (DTA) to determine the appropriate calcination temperature range. This step provided information on the phase transitions and thermal behavior of the sample, which was crucial in determining the optimum calcination temperatures. The TGA

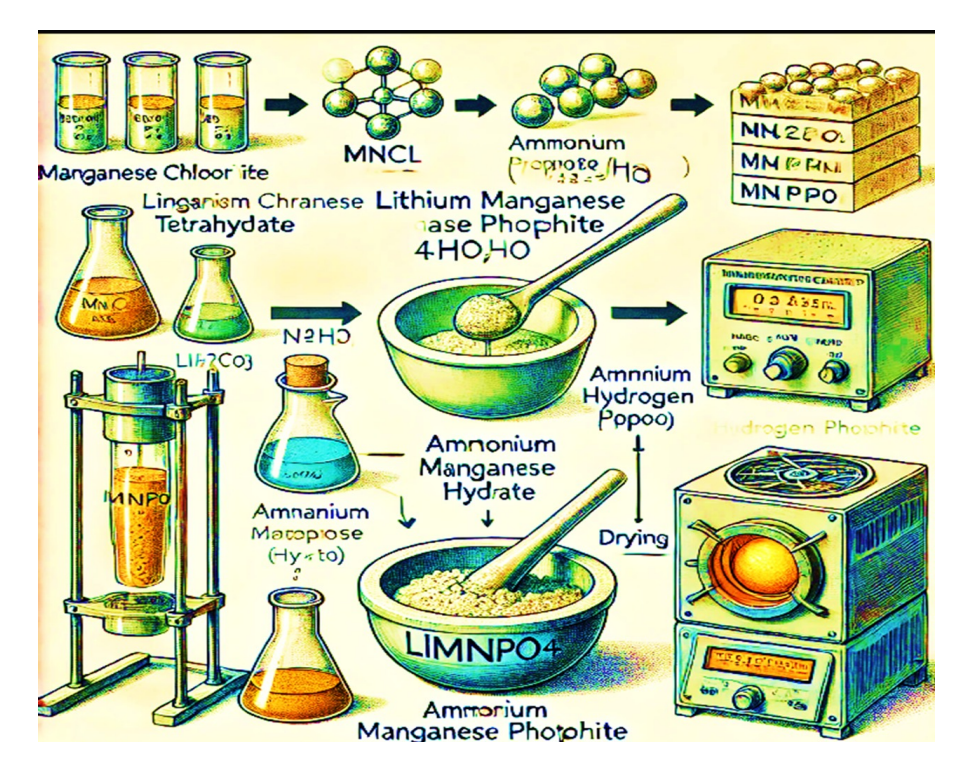


Fig. 1: Graphical representation of the synthesis process of LiMnPO₄.

data allowed for the identification of the temperature at which the reaction and phase change occurred. Based on the TGA results, the remaining mixture was divided into three portions, and each portion was calcined in alumina crucibles at different temperatures to optimize the formation of LiMnPO₄: One portion was calcined at 600 K for 2 hours, a second portion was calcined at 730°C for 2 hours and the third portion was calcined at 840°C for 2 hours.

All calcination steps were carried out in a muffle furnace, with the heating rate maintained at 5° C per minute, and the samples were kept at their respective temperatures for 2 hours. After calcination, the LiMnPO₄ product was allowed to cool to room temperature. After calcination, the LiMnPO₄ samples were washed with deionized water several times to remove any residual reactants or impurities. The washed samples were then dried at 110° C overnight in an oven to ensure complete water removal and any volatile impurities. The final product was stored in a desiccator to maintain dryness until further characterization or investigation. All these steps have been summarized graphically in Fig.1, which was generated using an AI machine.

2.2 Characterization Tools

The X-ray diffraction patterns (XRD) were performed using the X-ray diffraction (XRD), Philips PW1710 with CuK α radiation (wavelength = 1.540598 Å). A PerkinElmer Spectrum 100 instrument with a universal attenuated total reflectance (UATR) accessory was used to collect Fourier-Transform Infrared (FTIR) data in the range from 400 cm⁻¹ to 4000 cm⁻¹ with a resolution of 4 cm⁻¹. The calculated average of 20 scans was used as a final result per sample.

The crystallization kinetics of $As_{37.5}Se_{37.5}Ag_{25}$ glass were investigated using a Shimadzu-50 Differential Scanning Calorimeter (DSC) with an accuracy of \pm 0.1 K. Each sample was heated from 300 K to 1000 K at a constant heating rate of ($5 \le \beta \le 25$ K min⁻¹). The crystallization peaks T_p were determined using the micro-processor of the thermal analyzer.

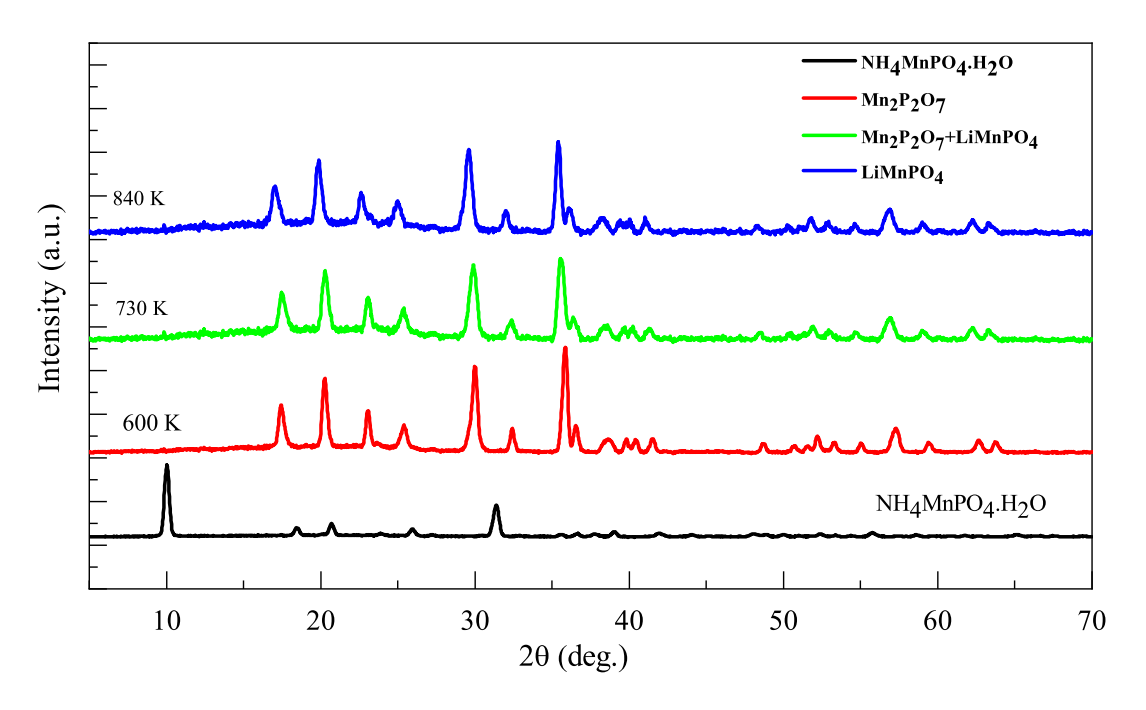


Fig. 2: XRD patterns

3 Results and Discussion

3.1 Spectral characterization: XRD & FTIR

Figure 2 depicts the XRD patterns of NH₄MnPO₄ · 2H₂O (black line, unheated), Mn₂P₂O₇ (red line, heated to 600 K), LiMnPO₄ (green line, heated to 730 K), and LiMnPO₄ (blue line, heated to 840 K). This image shows that each state has a unique crystal structure, confirming the heating effect impacting on NH₄MnPO₄ · 2H₂O as well as the thermal transformations to LiMnPO₄.

Figure 3 depicts the normalized XRD patterns, which show a strong match between samples 3 and 4, confirming the structural stability of the LiMnPO₄ structure. On the other hand, the observed shift in the peak location of NH₄MnPO₄ to higher 2-theta values caused by heating can be explained by a change in the unit cell characteristics between NH₄MnPO₄ · 2H₂O, Mn₂P₂O₇, and LiMnPO₄. This observation is obvious, as shown in Table 2, which compares the XRD parameters of NH₄MnPO₄ and LiMnPO₄ after being matched to the standard XRD data foundation [10,11,12].

Table 2: XRL) parameters of	NH_4MnPO_4	and LiMnPO $_4$.
--------------	-----------------	--------------	-------------------

	Sys.	Space group	Space group No.	a, pm	b, pm	c, pm	V, pm ³	Z
NH ₄ MnPO ₄ .2H ₂ O	Orthorhombic	Pmn 21	31	5.68	8.78	4.88	243.37	2
NH ₄ MnPO ₄ .2H ₂ O	Orthornomore	Pmn	62	4.711	10.374	6.038	295.09	4

Figure 4 shows FTIR plots for NH₄MnPO₄ · 2H₂O (black line, unheated), Mn₂P₂O₇ (red line, heated to 600 K), LiMnPO₄ (green line, heated to 730 K), and LiMnPO₄ (blue line, heated to 840 K). Figure 4 depicts differences in the vibrational modes of the NH₄MnPO₄ · 2H₂O and LiMnPO₄ phases, where some vibrational modes appeared in lowwavenumber regions ($\leq 1600 \text{ cm}^{-1}$), whereas others disappeared in high-wavenumber regions ($4000 \text{ cm}^{-1} - 1600 \text{ cm}^{-1}$).

Figures 5(a-d) show the deconvolution of the FTIR charts for all samples, individually. As shown in Figure 5a, NH₄MnPO₄ · 2H₂O reflects the characteristic stretching modes of H–O, N–H, and P–O, where the water bonding as well as O-H stretching vibration cover the range 1750-4000 cm⁻¹, which implies the presence of crystalline hydrate. Several strong and sharp absorption bands from 400 to 1600 cm^{-1} may be due to the stretching modes of the group [12,13]. The peaks between 500 and 1050 cm^{-1} are due to PO₄ vibrations [14,15].

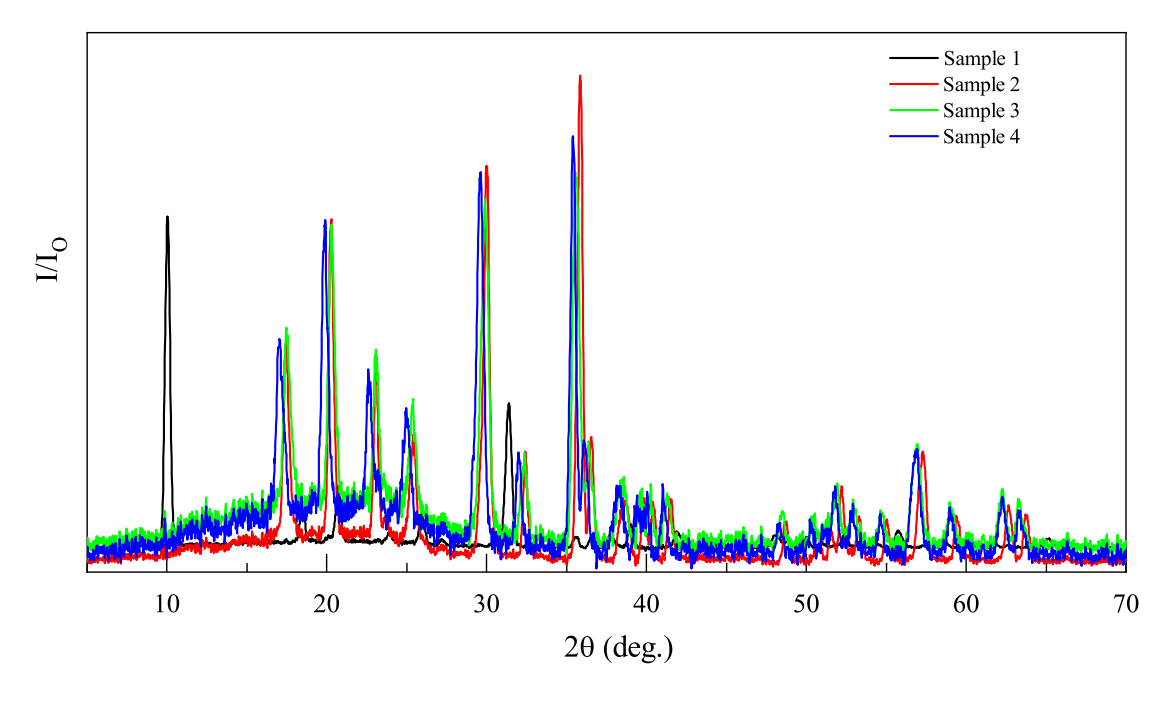


Fig. 3: Normalized XRD Patterns of all samples

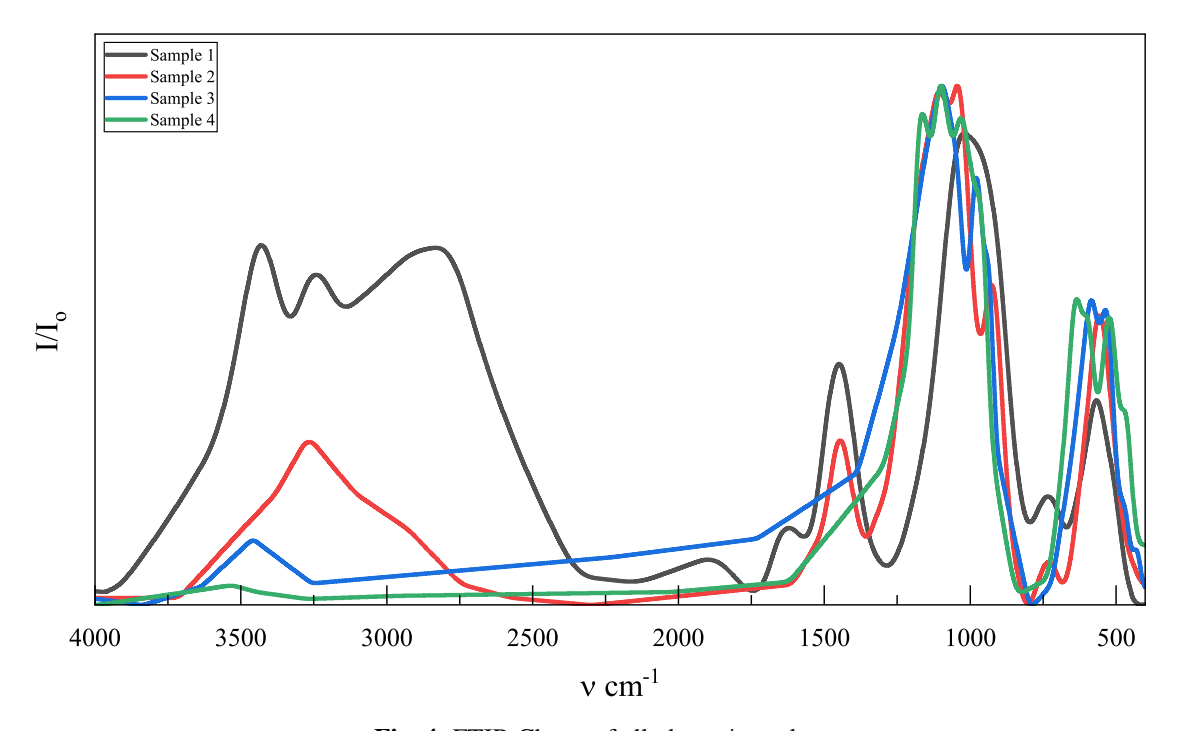


Fig. 4: FTIR Charts of all phases/samples



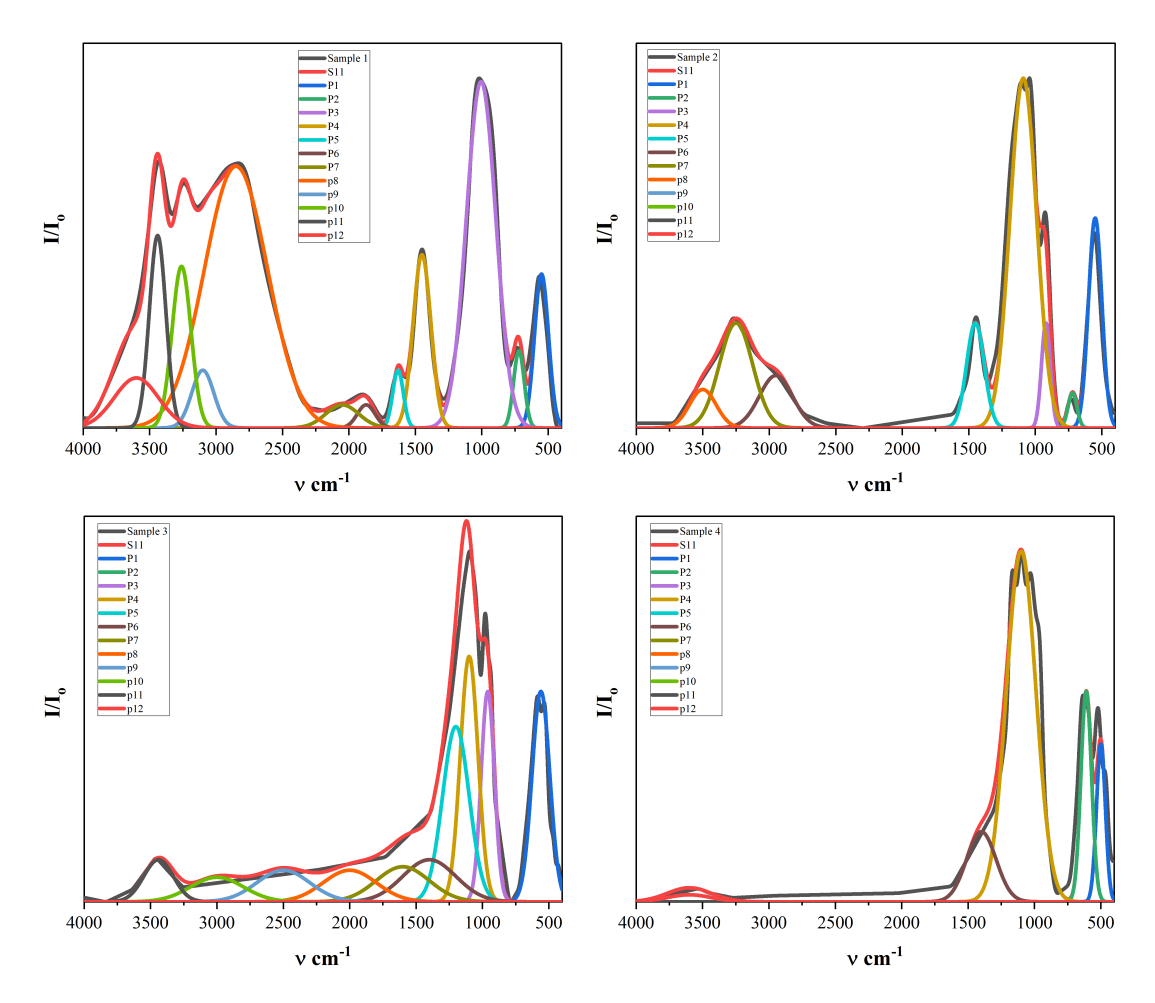


Fig. 5: FTIR Chart of sample 1 with its deconvolution curves

Additionally, vibrations at 1450 cm^{-1} and a broad band at $2850-3260 \text{ cm}^{-1}$ indicate the existence of $(NH_4)^+$ [14]. Figure 5b, $Mn_2P_2O_7$, shows the same trend as in Figure 5a, but the peak at 1005 cm^{-1} moved to a new position at 1090 cm^{-1} , which characterizes the formation of $Mn_2P_2O_7$ phase [16]. Also, Figure 5b shows a decrease in the vibration absorption amplitude of OH groups. This decrease reflects a reduction in the number or activity of hydroxyl (OH) groups in the sample, which may hint at phase transition activity upon heating, as expected. Figures 5(c-d) are identical, indicating that the vibration modes of OH groups and water disappear by heating to high temperatures. Also, the peak indicating the $Mn_2P_2O_7$ phase has vanished.

3.2 Thermal characterization: Solid-state solution & Conversion

Figure 6 depicts the DTA curve for the solid solution $NH_4MnPO_4 \cdot H_2O$ and Li_2CO_3 at a heating rate of 5 K min⁻¹. It shows a pronounced endothermic peak around 477 K, which could be due to either water loss during the conversion process or ammonia gas emission. Also, Figure 6 shows two different-magnitude exothermic peaks at 477 and 723 K, which can be attributed to thermal breakdown. These peaks frequently indicate energy release during the compound's thermal disintegration [17,18].

On the other hand, the TGA curve, Figure 7, shows that the mass of the $NH_4MnPO_4 \cdot H_2O$ and Li_2CO_3 gradually reduces with increasing temperature and drops sharply between 419 K and 515 K due to dehydration and ammonia leakage. The decreasing rate then slowed around 515 K and plateaued at about 765 K, showing that the removal of water and ammonia is nearly complete [19].

Many factors motivate kinetic investigations, including improving methods for detecting decomposition or reaction rates, identifying intermediate phases or products during thermal treatment, and investigating new reaction routes or

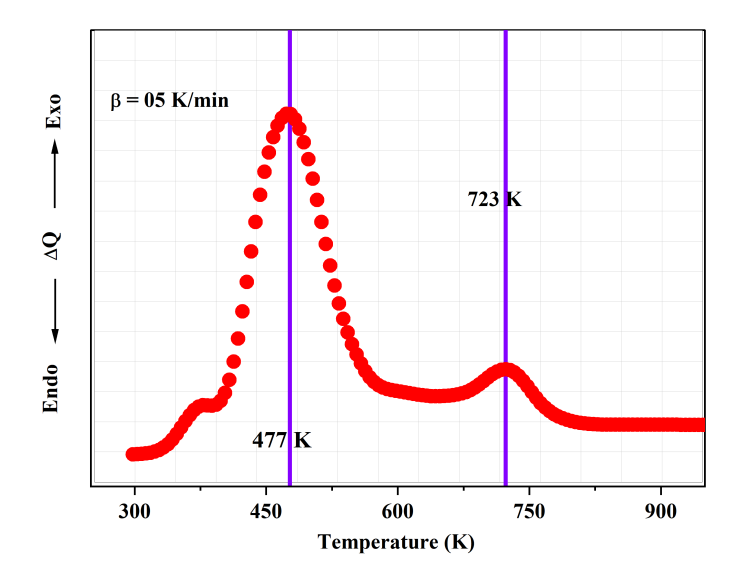


Fig. 6: DTA curve of the solid solution NH₄MnPO₄·H₂O and Li₂CO₃ at a heating rate of 5 K min⁻¹.

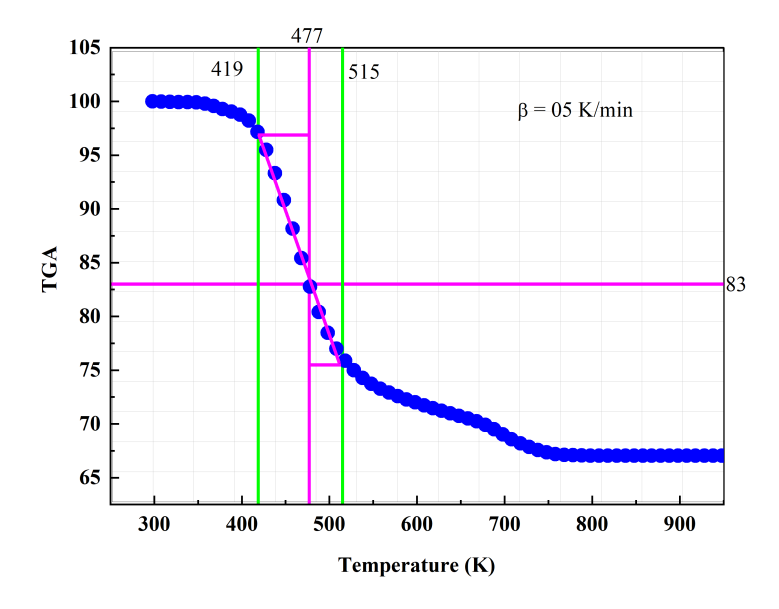


Fig. 7: TGA curves of the solid solution NH₄MnPO₄·H₂O and Li₂CO₃ at a heating rate of 5 K min⁻¹.

variables that influence stability or decomposition rates. Generally, kinetic investigations are crucial for understanding the fundamental mechanics of reactions or transformations.

In this context, the activation energies for the thermal breakdown of the mixture $NH_4MnPO_4 \cdot H_2O$ and Li_2CO_3 were extracted using the DTA technique in static air, with heating rates of 5, 10, 15, 20, and 25 K/min, as shown in Figure 8. Figure 8 shows evident endothermic peaks that represent discrete dehydration-related thermal events and subsequent phase changes.

Analyzing the temperature range and amplitude of these peaks can provide information on stability, phase transitions, and potential uses. The first exothermic peak is often associated with the compound's dehydration, in which NH_3 , H_2O , and CO_2 are released, resulting in bond breakage and a more stable anhydrous phase, as well as heat release. The second exothermic peak could signal a transition to the more stable $LiMnPO_4$ new phase, which could include the rearrangement of the lithium, manganese, and phosphate ions in the solid state, further stabilizing the material and releasing heat.

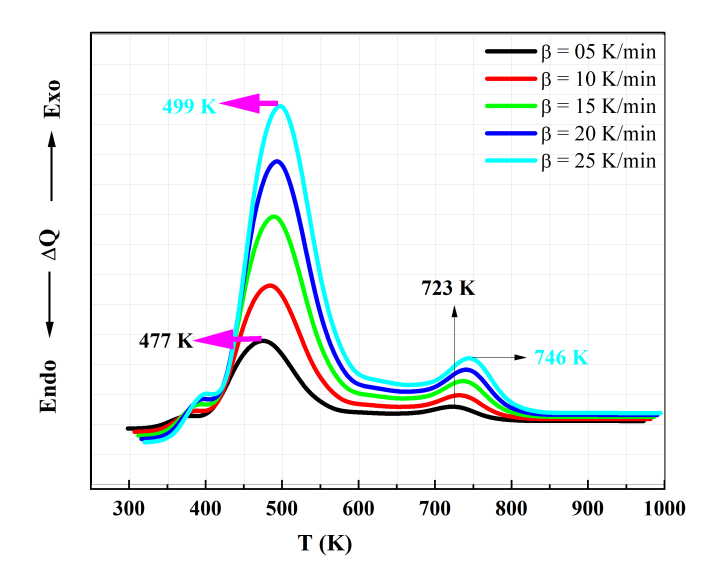


Fig. 8: DTA thermograms of NH₄MnPO₄·H₂O and Li₂CO₃ at different heating rates.

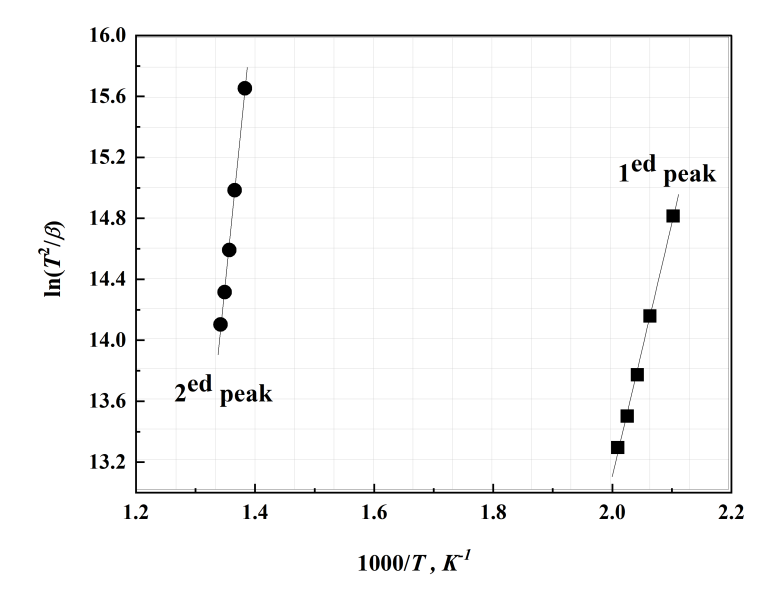


Fig. 9: $\ln \left(\frac{T_{\chi,i}^2}{\beta_i} \right)$ against for NH₄MnPO₄·H₂O, Li₂CO₃

Also, Figure 8 demonstrates how the centers of the conversion peaks migrate to higher values as the heating rate increases. These changes arise because the conversion process is kinetically directed rather than thermodynamically driven in non-isothermal environments. This behavior is characteristic of non-isothermal conversions and is used to determine the kinetic parameters [20,21]. Based on such a result, Kissinger's approach developed by Vázquez et al. [22,23], Eq. (1), has been used to evaluate activation energy for the conversion process.

The activation energy, E_c , and the frequency factor, K_0 , were evaluated by least squares fitting method of Eq. (1), where $\ln(T_p^2/\beta)$ versus $(1000/T_p)$ has been determined experimentally and then plotted for the mixture NH₄MnPO₄ · H₂O and Li₂CO₃, showing the straight regression line in Fig. 9. The slopes of the curves in Fig. 9 determined the activation energy values using the two DTA exothermic peaks as 137.95 and 318.70 kJ/mol, respectively.

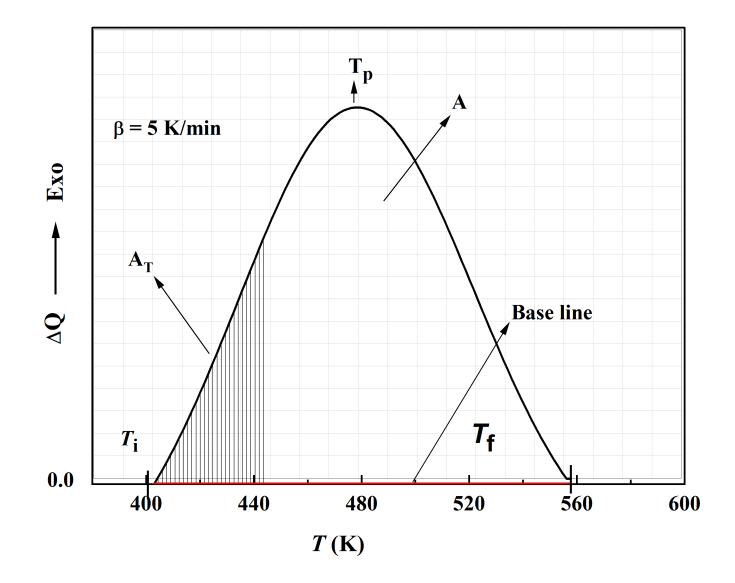


Fig. 10: DTA traces for the first conversion peak NH₄MnPO₄·H₂O, Li₂CO₃ at $\beta = 5$ K/min.

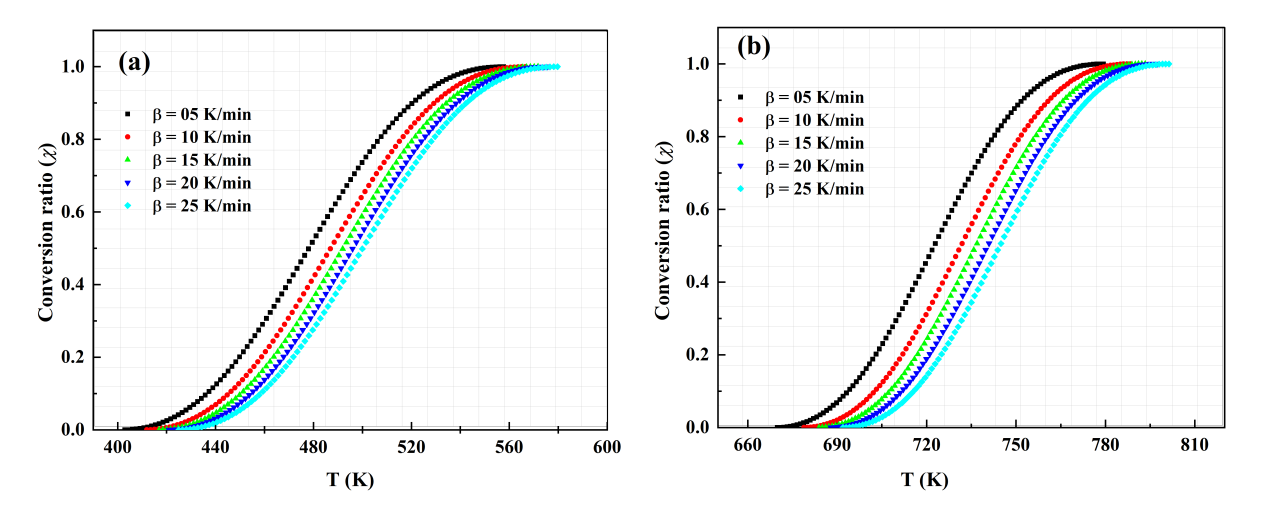


Fig. 11: Conversion ratio against temperature for different heating rates for (a) first peak and (b) second peak.

$$\ln\left(\frac{T_p^2}{\beta}\right) = \frac{E_c}{RT_p} + \ln\left(\frac{E_c}{RK_0}\right) \tag{1}$$

Many factors can influence the phase-to-phase conversion ratio, including temperature, cooling rate, and material characteristics. In the phase conversion process, the conversion ratio χ at a temperature T represents the proportion of a material that has been converted. Figure 10 shows the DTA traces for the first conversion peak of NH₄MnPO₄ · H₂O and Li₂CO₃ at $\beta = 5$ K/min Eq. (2) was used to calculate the conversion ratio χ , where A is the total area of the exothermic peak between the beginning of conversion temperature (T_i) and the full conversion temperature (T_i), and T_i :

$$\chi = \frac{A_T}{A} \tag{2}$$

The graphical representation of the conversion ratio displays the typical sigmoid curve as a function of temperature for the first peak of $NH_4MnPO_4 \cdot H_2O$ and Li_2CO_3 at varied heating rates, as illustrated in Fig. 11 (for both first and



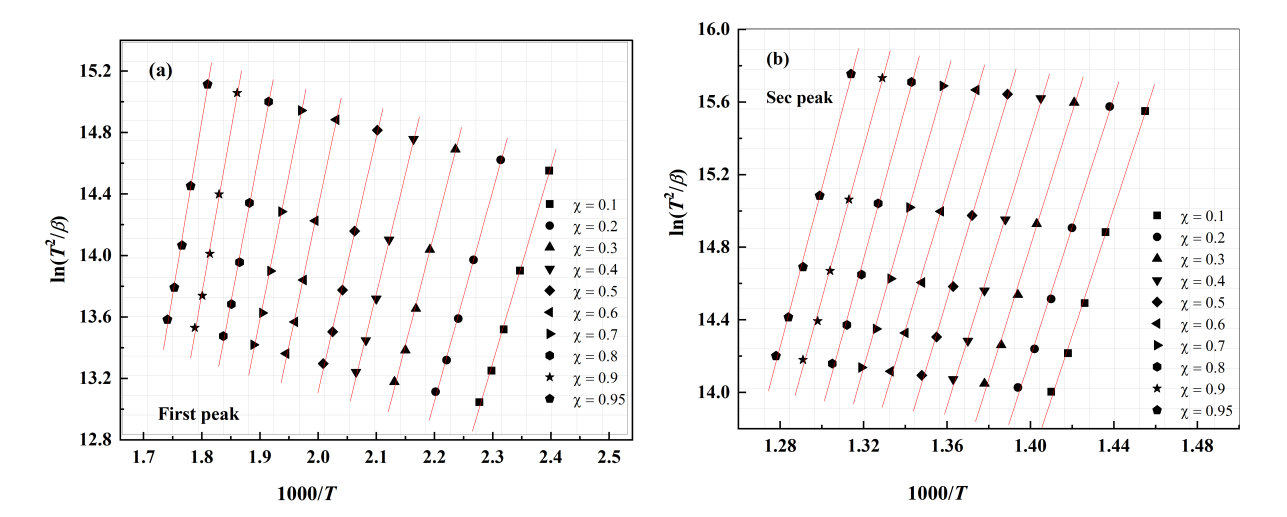


Fig. 12: $\ln\left(\frac{T_{\chi,i}^2}{\beta_i}\right)$ against for each conversion level $0.1 \le \chi \le 0.9$ for both first peak (a) and second peak (b).

second peaks), where conversion rates can be determined by dividing the ordinates of the DTA curve by the peak's total area. It can be observed that the heating rate had little effect on the center of the conversion ratio curve versus the absolute temperature, as illustrated in Fig. 11. However, the area under the curve decreased as the heating rate increased. The reduction in the region beneath the converted ratio peak with increasing heating rate suggests that the conversion process is impeded by the rapid thermal conditions.

$$\ln\left(\frac{T_{\chi_j}^2}{\beta_j}\right) = \text{Constant} - \frac{E_c(\chi)}{RT_{\chi_j}}$$
(3)

One of the most widely used in non-isothermal kinetics to determine the activation energy of a reaction is the isoconventional methods of the Kissinger-Akahira-Sunose approach [24,25] provided by Eq. (3) which was applied in the current study to determine the activation energy of conversion for both the first and second peaks, as shown in Figs. 12(a,b). On the other side Figs. 13(a,b) depict the plot of $E_c(\chi)$ values against conversion (χ) based on the slope of the straight lines. $E_c(\chi)$ increases as χ rises from 0.1 to 0.9. The values obtained for the activation energies of conversion E_c of NH₄MnPO₄·H₂O, Li₂CO₃ are consistent with those obtained using iso-conventional methods. On the same context the pre-exponential factor K_0 was obtained and plotted in Figs. 14(a,b) for first and second peaks, respectively.

By inspecting Figs. 13(a,b) and 14(a,b), the observed increase in activation energies vs. the conversion ratio indicates that as the conversion process progresses, it gets more energetically demanding, reflecting changes in the material's physical and thermodynamic properties. While the frequency factor decreases with increasing conversion ratio may declares that the conversion process becomes less efficient, reflecting changes in molecular interactions and the dynamic environment as $NH_4MnPO_4 \cdot H_2O$, Li_2CO_3 converts to $LiMnPO_4$ state [26,27].

Figures 13(a,b) show that the conversion energy of the second phase is greater than that of the first phase. In this sense, the lower energy of the first phase means that it is simpler to develop under specified conditions, despite the fact that the second phase is more energy stable. This underlines the relationship between thermodynamics and kinetics in crystallization processes. This means that the appearance of the first phase may be governed by kinetic factors rather than thermodynamic stability [28, 29, 30].

The theoretical basis for the interpreting of the DTA results is provided by the formal theory of transformation kinetics as developed by Johnson and Mehl [31] and Avrami [32,33]. The ratio between the ordinates of the DTA curve and the total area of the peak gives the corresponding conversion rates, as shown in Fig. 10. Such a ratio makes it possible to build the curves of the exothermal peaks as depicted in Figs 15(a,b), which shows that the change in $(d\chi/dt)_p$ values with heating increased as the heating rate was increased, which has been widely discussed in the literature [34]. In such context, based on the experimental data of the $(d\chi/dt)_p$, the kinetic exponent n, Eq. (4), was extracted using five experimental heating rates for the conversion peaks, and listed in Table 3.



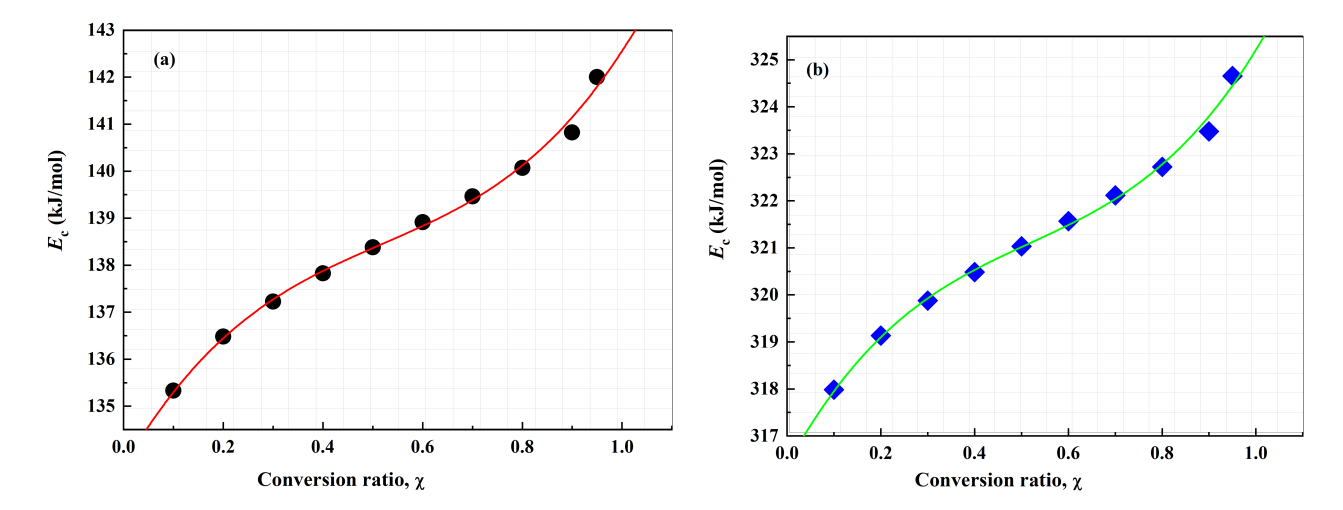


Fig. 13: $E_c(\chi)$ against the conversion fraction (χ) , based on 1st peak (a) and 2nd peak (b).

Table 3: Maximum conversion rate, kinetic exponent n, and average kinetic exponent with different heating rates.

	First peak		Second peak		
β (K/min)	$(d\chi/dt) \times 10^{-3} \text{ s}^{-1}$	n	$(d\chi/dt) \times 10^{-3} \text{ s}^-$	n	
5	5.79	2.554	4.9	2.465	
10	11.2	2.571	9.61	2.482	
15	16.4	2.567	14.1	2.478	
20	21.4	2.569	18.6	2.48	
25	26.3	2.563	22.9	2.474	
$\langle n \rangle$. 2555		2.466		

$$\left(\frac{d\chi}{dt}\right)_p = 0.37\,\beta\,n\,\frac{E_c}{RT_p^2}\tag{4}$$

As seen in Table 3, the mean value of kinetic exponent n, at each heating rate, is close to 3 which may nominate a single conversion mechanism for the conversion of NH₄MnPO₄·H₂O, Li₂CO₃ to LiMnPO₄. Such a value is consistent with the mechanism of volume nucleation with three-dimensional growth for all different compositions [35]. From another view, when non-integer absolute values of n are considered, it is possible to conclude that two conversion mechanisms exist (two- and three-dimensional growth). These mechanisms operate concurrently throughout the conversion transformation of the NH₄MnPO₄·H₂O, Li₂CO₃ solid solution [36, 37].

3.3 Sestak-Berggren (SB) modelling

The Šesták-Berggren (SB) model, Eq. (5), is commonly used to describe complex solid-state processes in materials science. It offers a versatile mathematical framework for capturing the reaction process using empirical parameters. The SB model is very useful for studying functionalized materials since it can handle non-linear and multi-step reaction processes, making it appropriate for thermochemical and structural changes [38,39]. In the present study, the theoretical DTA curves based on the SB model are derived using Eq. (5d) [40].

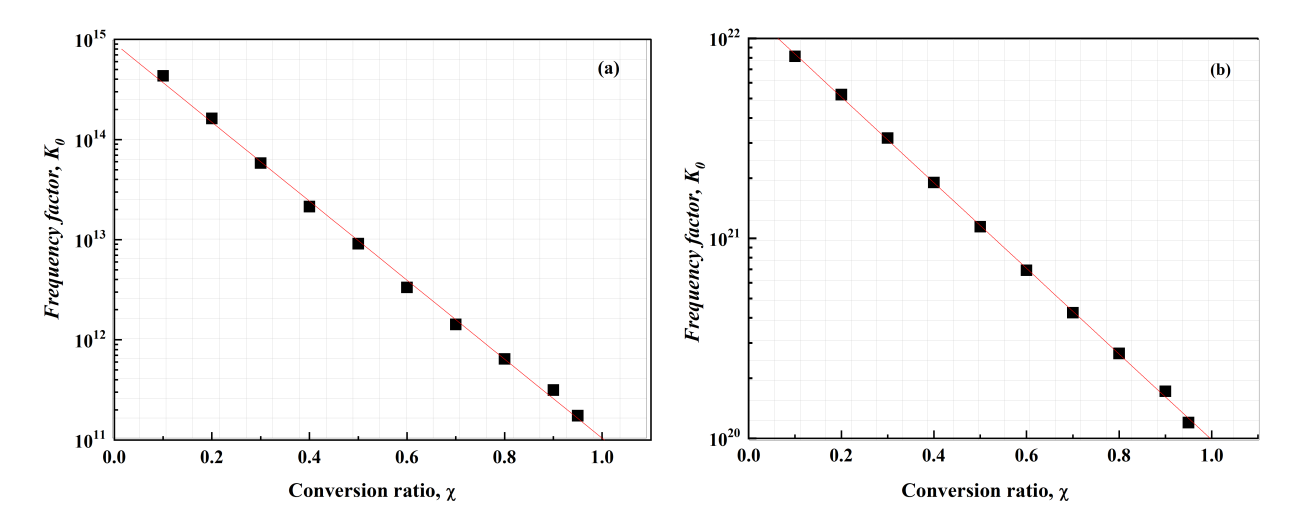


Fig. 14: Frequency factor K_0 against the conversion ratio (χ) , based on 1st and 2nd peaks.

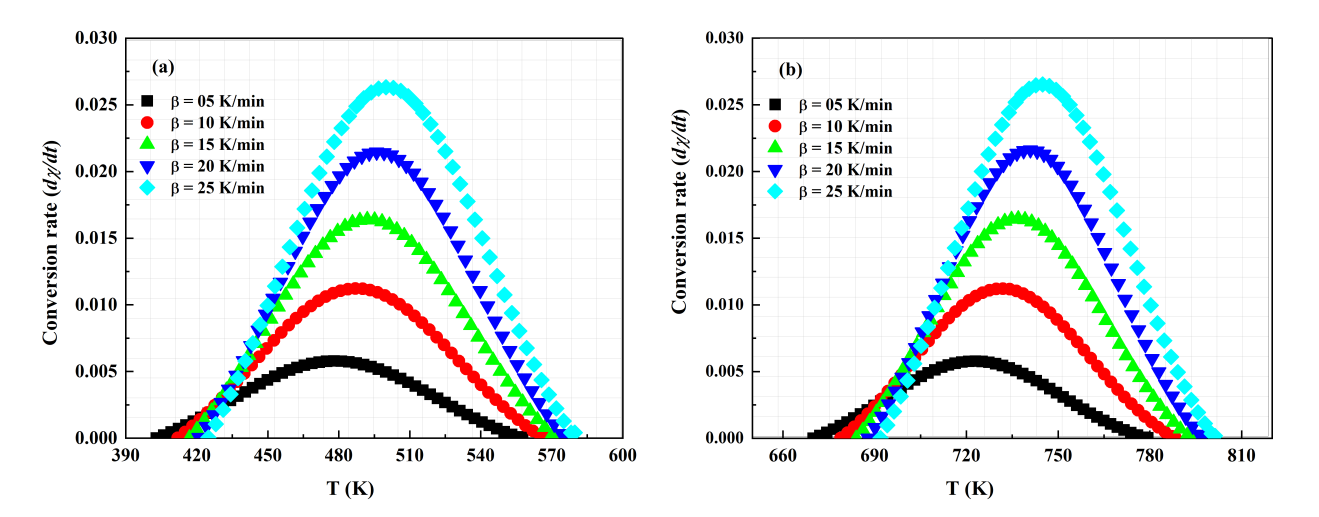


Fig. 15: Conversion rate versus absolute temperature for 1st and 2nd peaks.

$$\frac{d\chi}{dt} = K_0 e^{-\frac{E_a}{RT}} \chi^m (1 - \chi)^n f(T)$$

$$\frac{d\chi}{dt} = K(T) f(\chi) e^{-\frac{E_a}{RT}}$$
(5b)
$$K(T) = K_0 f(T)$$
(5c)

$$\frac{d\chi}{dt} = K(T)f(\chi)e^{-\frac{E_a}{RT}} \tag{5b}$$

$$K(T) = K_0 f(T) \tag{5c}$$

$$f(\chi) = \chi^m (1 - \chi)^n \tag{5d}$$

Figures 16(a,b) show a comparison of experimental and estimated DTA curves for the two crystalline peaks of NH₄MnPO₄·H₂O, Li₂CO₃. Where the DTA curves calculated using the SB model correlate well with the experimental ones at all heating rates. The validity of Eq. (5d) for characterizing the DTA data of the examined glass can be defined as the complete nucleation process that happens during the early phases of the transformation and is minimal subsequently [41]. This so-called site saturation assumption is fundamental to this conversion process since the conversion rate is only known by the temperature and has little influence on the thermal history [42]. Thus, the SB kinetic model can be used to quantitatively describe the crystallization process of our studied composition.



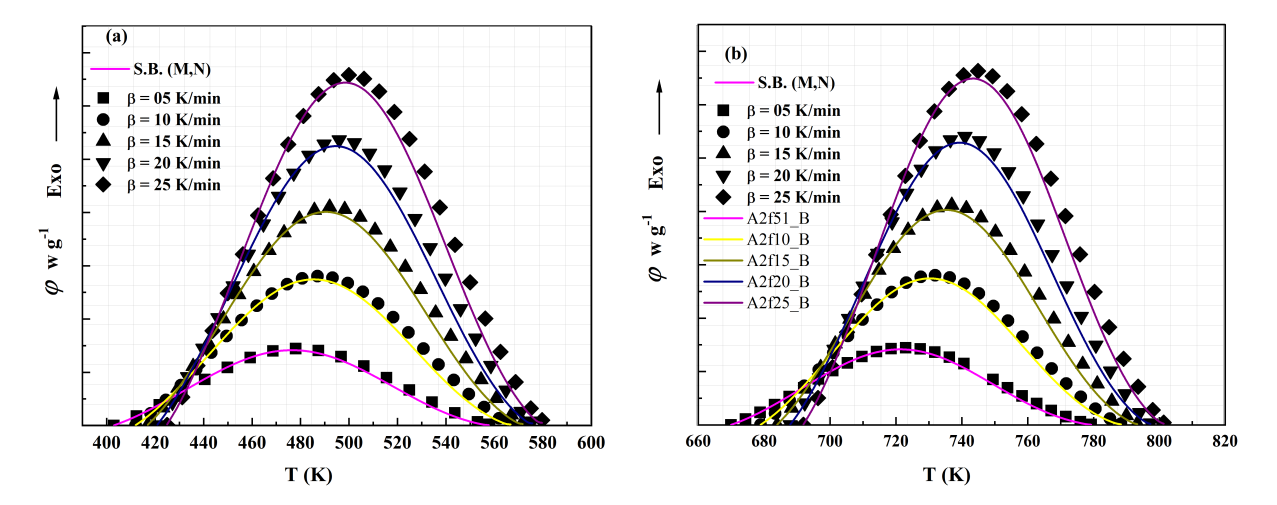


Fig. 16: Comparison of the experimental DTA data with those calculated using the SB model, at different heating rates of the first and second conversion peaks, respectively.

The kinetic parameters m and n of the S.B model determine the relative contributions of the acceleration and deceleration fractions of the conversion mechanism. The two-parameter autocatalytic model has physical meaning only for (m < 1). To determine the m and n parameters, apply the conversion corresponding to the maximum of the $y(\chi)$ and $z(\chi)$ functions, Eqs. (6) and (7), where φ is the heat flow and ΔH is the crystallization enthalpy [43].

$$y(\chi) \approx \varphi e^{-\frac{E_c}{RT}} \tag{6}$$

$$z(\chi) \approx \varphi T^2$$
 (7)

$$\varphi = \Delta H e^{-\frac{E_c}{RT}} f(\chi) \tag{8}$$

The functions $z(\chi)$ and $y(\chi)$ were plotted versus the conversion ratio χ for different heating rates as shown in Figs. 17(a,b) for the first and second peaks of the conversion process. It is obvious that the maximum values of $z(\chi)$ and $y(\chi)$ functions increased as the heating rate was increased from 5 to 25 K min⁻¹. The conversion χ_{max} which corresponds to the maximum of $y(\chi)$ and $z(\chi)$ functions was used to determine the m and n parameters based on the following relation, Eq. (9) [43].

$$\ln\left(\varphi e^{\frac{E_c(\chi)}{RT}}\right) = \ln(\Delta HA) + n\ln\left[\chi^{\frac{m}{n}}(1-\chi)\right] \tag{9}$$

where

$$\frac{m}{n} = \frac{\chi_{\text{max}}}{1 - \chi_{\text{max}}}, \quad 0.2 \le \chi \le 0.8$$

By plotting the term $\ln\left(\varphi e^{\frac{E_c(\chi)}{RT}}\right)$ versus the term $n\ln\left[\chi^{\frac{m}{n}}(1-\chi)\right]$, as shown in Figures 18(a, b), the values of both m and n were obtained as well as the value of enthalpy ΔH , as summarized in Table 4 for both conversion peaks.



Table 4: Conversion	enthalny (ΛH)	n/n m a	and n of both a	conversion i	neaks at differen	t heating rates
Table 4. Conversion	Circiaipy (211), 1	11 / 11, 111, a	ma n or bom v		peaks at afficient	t meating rates.

First Peak							
$\beta \left(\text{Kmin}^{-1} \right)$	$\beta \left(\text{Kmin}^{-1} \right) \Delta H(J/g)$		n	m			
5	10.2	0.245	1.109	0.272			
10	20.3	0.276	1.22	0.336			
15	40.7	0.271	1.316	0.357			
20	66.2	0.267	1.394	0.372			
25	81.3	0.263	1.466	0.386			
Second Peak							
	$\Delta H(J/g)$	m/n	m	n			
5	63.2	0.45	1.109	0.499			
10	70.6	0.506	1.22	0.617			
15	81.8	0.498	1.316	0.655			
20	97.4	0.49	1.394	0.683			
25	109	0.483	1.466	0.707			

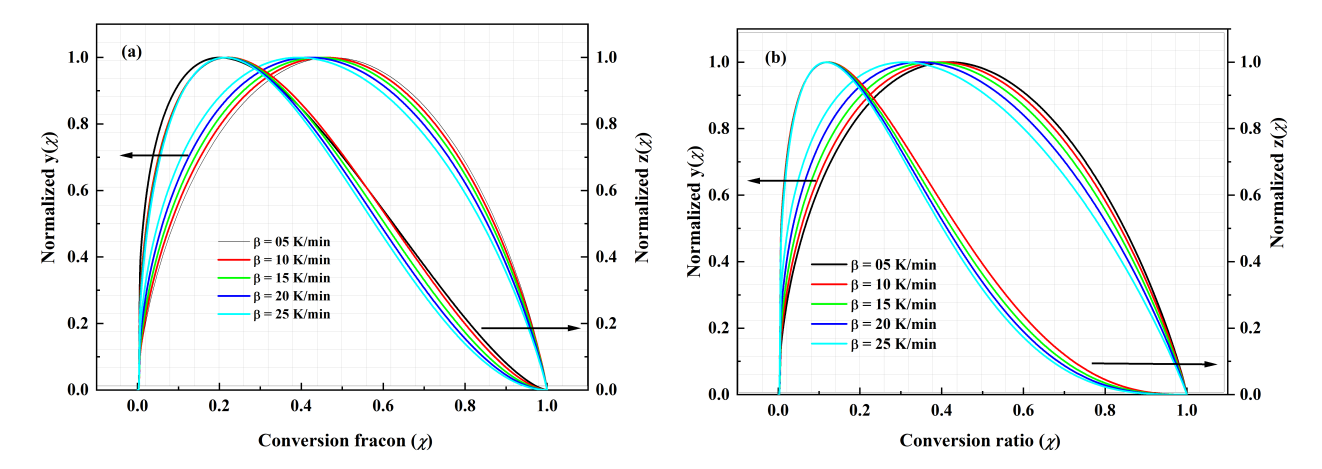


Fig. 17: Normalized $y(\chi)$ and $z(\chi)$ functions versus the conversion (χ) of the first and second conversion peaks.

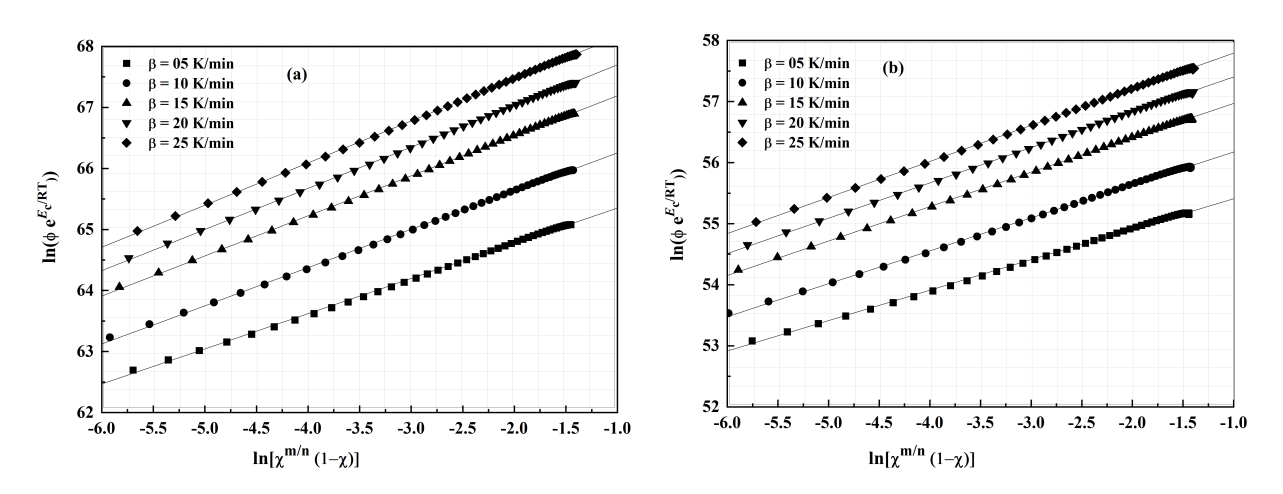


Fig. 18: Plot of $\ln\left[\phi\exp(E_c(\chi)/RT)\right]$ versus $\ln\left[\chi^{m/n}(1-\chi)\right]$ at different heating rates of the first and second crystallization peaks, respectively, of the studied glass.



4 Conclusion

This study successfully synthesized lithium manganese phosphate (LiMnPO₄) through a controlled solid-state reaction, emphasizing the critical influence of synthesis and thermal treatment parameters on phase formation and stability. The multi-step process, involving the initial precipitation of NH₄MnPO₄·H₂O followed by its calcination with lithium carbonate, yielded phase-pure LiMnPO₄ when optimized calcination conditions were applied. Thermal analysis using TGA and DTA identified key transformation temperatures, with distinct phase transitions verified by XRD and FTIR spectroscopy. The kinetic investigations, employing Kissinger-Akahira-Sunose (KAS) and Šesták-Berggren (SB) models, provided a detailed understanding of the conversion mechanisms and activation energies. The results demonstrated that the thermal decomposition and phase transition processes are governed by non-isothermal kinetics, with three-dimensional nucleation and growth as the predominant mechanisms. The activation energy values and kinetic parameters derived from the study offer valuable insights into the material's thermal behavior, supporting the optimization of synthesis strategies for high-purity LiMnPO₄. Overall, the integration of thermal analysis, structural characterization, and kinetic modeling has deepened our understanding of the NH₄MnPO₄·H₂O to LiMnPO₄ conversion process. This comprehensive approach not only enhances the potential for scalable production of LiMnPO₄ but also contributes to the broader field of functional materials development, particularly for energy storage applications.

Conflict of Interest

The authors declare that there is no conflict of interest regarding the publication of this paper.

References

- [1] M. Brown, M. Maciejewski, S. Vyazovkin, R. Nomen, J. Sempere, A. a. Burnham, J. Opfermann, R. Strey, H. Anderson, A. Kemmler *et al.*, Computational aspects of kinetic analysis: part a: the ictac kinetics project-data, methods and results, *Thermochimica Acta* **355**(1-2) (2000) 125–143.
- [2] R. L. Gibson, M. J. Simmons, E. H. Stitt, J. West, S. K. Wilkinson and R. W. Gallen, Kinetic modelling of thermal processes using a modified sestak-berggren equation, *Chemical Engineering Journal* **408** (2021) p. 127318.
- [3] R. L. Gibson, M. J. Simmons, E. H. Stitt, J. West, S. K. Wilkinson and R. W. Gallen, Kinetic modelling of thermal processes using a modified sestak-berggren equation, *Chemical Engineering Journal* **408** (2021) p. 127318.
- [4] P. J. Barrie, Analysis of temperature programmed desorption (tpd) data for the characterisation of catalysts containing a distribution of adsorption sites, *Physical Chemistry Chemical Physics* 10(12) (2008) 1688–1696.
- [5] S. Ashtekar, S. V. Chilukuri and D. K. Chakrabarty, Small-pore molecular sieves sapo-34 and sapo-44 with chabazite structure: a study of silicon incorporation, *The Journal of Physical Chemistry* **98**(18) (1994) 4878–4883.
- [6] F. Arena, R. Di Chio and G. Trunfio, An experimental assessment of the ammonia temperature programmed desorption method for probing the surface acidic properties of heterogeneous catalysts, *Applied Catalysis A: General* **503** (2015) 227–236.
- [7] J. Šesták and G. Berggren, Study of the kinetics of the mechanism of solid-state reactions at increasing temperatures, *Thermochimica Acta* **3**(1) (1971) 1–12.
- [8] S. Vyazovkin, A. K. Burnham, J. M. Criado, L. A. Pérez-Maqueda, C. Popescu and N. Sbirrazzuoli, Ictac kinetics committee recommendations for performing kinetic computations on thermal analysis data, *Thermochimica acta* **520**(1-2) (2011) 1–19.
- [9] R. L. Gibson, M. J. Simmons, E. H. Stitt, J. West, S. K. Wilkinson and R. W. Gallen, Kinetic modelling of thermal processes using a modified sestak-berggren equation, *Chemical Engineering Journal* **408** (2021) p. 127318.
- [10] C. O. Björling and A. Westgren, Minerals of the varuträsk pegmatite: Ix. x-ray studies on triphylite, varulito, and their oxidation products, *Geologiska Föreningen i Stockholm Förhandlingar* **60**(1) (1938) 67–72.
- [11] P. J. Bridge and B. Robinson, Niahite—a new mineral from malaysia, Mineralogical Magazine 47(342) (1983) 79–80.
- [12] Q. Zhao, W. Mahmood and Y. Zhu, Synthesis of dittmarite/mg (oh) 2 composite coating on az31 using hydrothermal treatment, Applied Surface Science 367 (2016) 249–258.
- [13] M. Llusar, A. García, C. Gargori, R. Galindo, J. Badenes and G. Monrós, Synthesis of diphosphate mn2- xmgxp2o7 solid solutions with thortveitite structure: New pink ceramic dyes for the colouration of ceramic glazes, *Journal of the European Ceramic Society* **32**(4) (2012) 765–776.
- [14] J. Wu, A.-Q. Yuan, Z.-Y. Huang, Z.-F. Tong, J. Chen and R.-L. Liang, Thermochemical properties and decomposition kinetics of ammonium magnesium phosphate monohydrate, *Chinese Journal of Chemistry* **25**(1) (2007) 72–76.
- [15] T. Finch and J. Sharp, Chemical reactions between magnesia and aluminium orthophosphate to form magnesia-phosphate cements, Journal of materials science 24(12) (1989) 4379–4386.
- [16] M. V. Ramlogan and A. A. Rouff, An investigation of the thermal behavior of magnesium ammonium phosphate hexahydrate, Journal of Thermal Analysis and Calorimetry 123(1) (2016) 145–152.
- [17] L. R. Thompson and J. W. Davis, Exothermic reactions in thermal decomposition of manganese dihydrogen phosphate: Mechanisms and energy release, *Journal of Thermal Analysis and Calorimetry* 78(3) (2023) 1456–1465.



- [18] T. H. Nguyen and K. J. Lee, Thermal stability and decomposition kinetics of mn(h₂po₄)₂ · 2h₂o: An analysis of exothermic behavior, *Thermochimica Acta* **81**(1) (2022) 99–107.
- [19] Z.-h. ZHONG, Y. Juan *et al.*, Thermal decomposition of magnesium ammonium phosphate and adsorption properties of its pyrolysis products toward ammonia nitrogen, *Transactions of Nonferrous Metals Society of China* **25**(2) (2015) 497–503.
- [20] W. Steinmann, S. Walter, M. Beckers, G. Seide and T. Gries, Thermal analysis of phase transitions and crystallization in polymeric fibers, *Applications of Calorimetry in a Wide Context-Differential Scanning Calorimetry, Isothermal Titration Calorimetry and Microcalorimetry* (2013) 277–306.
- [21] S. Vyazovkin, Activation energies and temperature dependencies of the rates of crystallization and melting of polymers, *Polymers* **12**(5) (2020) p. 1070.
- [22] H. E. Kissinger, Reaction kinetics in differential thermal analysis, Analytical chemistry 29(11) (1957) 1702–1706.
- [23] J. Vazquez, P. Lopez-Alemany, P. Villares and R. Jimenez-Garay, Generalization of the avrami equation for the analysis of non-isothermal transformation kinetics. application to the crystallization of the cu0. 20as0. 30se0. 50 alloy, *Journal of Physics and Chemistry of Solids* **61**(4) (2000) 493–500.
- [24] T. Sunose and T. Akahira, Application of the kissinger-akahira-sunose method for kinetic analysis in non-isothermal decomposition studies, *Journal of Thermal Analysis and Calorimetry* **82**(2) (2024) 345–354.
- [25] A. Vazquez and J. Rodriguez, Kinetic analysis of thermal decomposition processes using the kissinger-akahira-sunose method: A comprehensive review, *Thermochimica Acta* 80(3) (2023) 512–520.
- [26] L. Zhang and T. Huang, Model-fitting approaches for estimating arrhenius parameters in crystallization kinetics: Activation energy and pre-exponential factor analysis, *Journal of Materials Science* **68**(3) (2023) 456–464.
- [27] J. Kim and S. Lee, Analyzing crystallization kinetics through model-fitting: Determination of activation energy and pre-exponential factors, *Thermochimica Acta* **79**(4) (2022) 675–683.
- [28] Thermodynamics and kinetics of crystallization in glassy systems, Journal of Non-Crystalline Solids 499 (2018) 136–144.
- [29] C. L. J. T. and A. J., Crystallization processes in multicomponent systems, Crystal Growth & Design 20(7) (2020) 4460-4469.
- [30] E. E. M. R. M. A. A., Phase transitions and nucleation in crystalline materials, Materials Today: Proceedings 47 (2021) 839-845.
- [31] M. Avrami, Kinetics of phase change. i: General theory, Journal of Chemical Physics 8 (1940) 212-224.
- [32] M. Avrami, Granulation, phase change, and microstructure: Kinetics of phase change. iii, *Journal of Chemical Physics* **9** (1941) 177–184.
- [33] Y. Q. Gao, W. Wang, F. Q. Zheng and X. Liu, On the crystallization kinetics of pd₈₀b₄si₁₆ glass, *Journal of Non-Crystalline Solids* **81** (1986) 135–139.
- [34] K. Matusita and S. Sakka, Kinetic study of crystallization of glass by differential thermal analysis: criterion on application of kissinger plot, *Journal of Non-Crystalline Solids* 38&39 (1980) 741–746.
- [35] H. Yinnon and D. R. Uhlmann, Applications of thermoanalytical techniques to the study of crystallization kinetics in glass-forming liquids, part i: Theory, *Journal of Non-Crystalline Solids* **54** (1983) 253–275, Title confirmed via multiple sources :contentReference[oaicite:0]index=0.
- [36] R. M. Mehra, G. Kaur, A. Ganjoo, R. Singh and P. C. Mathur, Effect of antimony doping on the transport properties of the glassy se_{80-x}te₂₀sb_x system, *Physica Status Solidi A* **124** (1991) K51–K53, Title confirmed via citation :contentReference[oaicite:1]index=1.
- [37] M. Mehdi, G. Brun and J. Tedenac, Crystallization kinetics of bulk amorphous (se₆₅te₃₅)_{100-x}sb_x, *Journal of materials science* **30**(20) (1995) 5259–5262.
- [38] P. Šimon, Forty years of the šesták-berggren equation, *Thermochimica Acta* 520 (2011) 156–157.
- [39] I. Rovenţa, L. A. Perez-Maqueda and A. Rotaru, Advancements in the integration and understanding of the šesták-berggren generalized conversion function for heterogeneous kinetics, *Journal of Thermal Analysis and Calorimetry* 149 (2024) 11493– 11506.
- [40] J. Málek, J. M. Criado, J. Šesták and J. Militký, The boundary conditions for kinetic models, *Thermochimica Acta* 153 (1989) 429–432.
- [41] J. W. Christian, The Theory of Transformations in Metals and Alloys, 2nd edn. (Pergamon Press, New York, 1975).
- [42] A. Calka and A. Radliński, Decoupled bulk and surface crystallization in pd₈₅si₁₅ glassy metallic alloys: Description of isothermal crystallization by a local value of the avrami exponent, *Journal of Materials Research* 3 (1988) 59–66.
- [43] J. Málek, Kinetic analysis of non-isothermal calorimetric data, Scientific Papers of the University of Pardubice 2 (1996) 177–209.